Lawrence Berkeley National Laboratory

LBL Publications

Title

Discovery of Fe—Ce Oxide/BiVO4 Photoanodes through Combinatorial Exploration of Ni—Fe—Co—Ce Oxide Coatings

Permalink

https://escholarship.org/uc/item/6b90n8jj

Journal

ACS Applied Materials & Interfaces, 8(36)

ISSN

1944-8244

Authors

Shinde, Aniketa

Guevarra, Dan

Liu, Guiji

et al.

Publication Date

2016-09-14

DOI

10.1021/acsami.6b06714

Peer reviewed

eScholarship.org Powered by the California Digital Library
University of California

ACS APPLIED MATERIALS & INTERFACES

Research Article

www.acsami.org

Discovery of Fe–Ce Oxide/$BiVO_4$ Photoanodes through Combinatorial Exploration of Ni–Fe–Co–Ce Oxide Coatings

Aniketa Shinde,[†] Dan Guevarra,[†] Guiji Liu,[‡] Ian D. Sharp,[‡] Francesca M. Toma,*[,‡] John M. Gregoire,*[,†] and Joel A. Haber*[,†]

[†]Joint Center for Artificial Photosynthesis, California Institute of Technology; Pasadena, California 91125, United States

[‡]Joint Center for Artificial Photosynthesis & Chemical Sciences Division, Lawrence Berkeley National Laboratory, Berkeley, California 94720, United States

Supporting Information

ABSTRACT: An efficient photoanode is a prerequisite for a viable solar fuels technology. The challenges to realizing an efficient photoanode include the integration of a semiconductor light absorber and a metal oxide electrocatalyst to optimize corrosion protection, light trapping, hole transport, and photocarrier recombination sites. To efficiently explore metal oxide coatings, we employ a high-throughput methodology wherein a uniform $BiVO_4$ film is coated with 858 unique metal oxide coatings covering a range of metal oxide loadings and the full $(Ni–Fe–Co–Ce)O_x$ pseudoquaternary composition space. Photoelectrochemical characterization of the photoanodes reveals that specific combinations of metal oxide composition and loading provide up to a 13-fold increase in the maximum photoelectrochemical power generation for oxygen evolution in pH 13 electrolyte. Through mining of the high-throughput data we identify composition regions that form improved interfaces with $BiVO_4$. Of particular note, integrated photoanodes with catalyst compositions in the range $Fe_{(0.4–0.6)}Ce_{(0.6–0.4)}O_x$ exhibit high interface quality and excellent photoelectrochemical power conversion. Scaled-up inkjet-printed electrodes and photoanodic electrodeposition of this composition on $BiVO_4$ confirms the discovery and the synthesis-independent interface improvement of $(Fe–Ce)O_x$ coatings on $BiVO_4$.

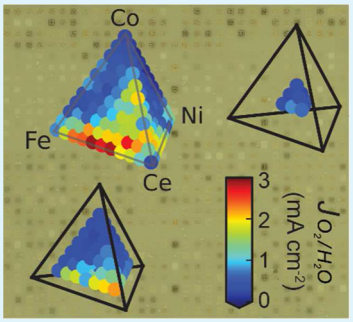

KEYWORDS: *solar fuels, materials integration, high-throughput experimentation, photoanode, oxygen evolution reaction*

1. INTRODUCTION

Conversion of solar energy to hydrogen via photoelectrochemical (PEC) water splitting offers a path toward storable and sustainable transportation fuels. The use of semiconductor/liquid junctions is particularly attractive for its simplicity and potential for low cost.[1] To achieve unassisted water splitting with high efficiency, a dual junction configuration is needed, in part to accommodate the large overpotential of the oxygen evolution reaction (OER).[1−3] For such an architecture, $BiVO_4$ has recently received significant attention as the photoanode light absorber in a dual-junction device,[4−7] as it possesses a bandgap near 2.5 eV and a valence band potential significantly more positive than the thermodynamic potential for OER.[8,9] However, the bare surface of $BiVO_4$ possesses high concentrations of electronically active defect states that diminish its photoelectrocatalytic activity for the OER.[10] Furthermore, the material suffers from chemical and photochemical instability under aqueous OER conditions.[11,12] Indeed, while strong alkaline conditions are usually preferred to reduce ohmic losses and prevent hydroxyl ion depletion during OER catalysis, they pose significant challenges for materials stability under operating conditions. Integration of alkaline stable oxygen evolution catalysts onto the surface of $BiVO_4$ can address these shortcomings.

We have recently described high-throughput methodologies and performance metrics for evaluation of catalyst/semiconductor assemblies as photoelectrodes, which demonstrated that specific compositions and loadings of mixed-metal oxide catalyst coatings can significantly improve the performance of $BiVO_4$-based photoanodes.[13] Herein, we extend this approach by integrating $(Ni–Fe–Co–Ce)O_x$ OER catalysts onto a thin film $BiVO_4$ light absorber and evaluating the resultant library of photoanode assemblies. This search reveals a new $(Fe–Ce)O_x$ catalyst composition and loading, which in scaled-up electrodes under standard AM1.5 test conditions outperforms the $(La–Co–Ce)O_x$ composition previously discovered through high-throughput methods using the same $BiVO_4$ substrate.[13] Moreover, the performance of this metal oxide coating is verified using photoanodic-electrochemical deposition (PED) as an alternate preparative method. Combinatorial variation of the catalyst composition and loading yields a wide range of photoanode properties, with composition trends notably different from those reported for the $(Ni–La–Co–Ce)O_x$ catalyst library on $BiVO_4$, providing additional insight into beneficial interfacial interactions.

Received: June 5, 2016
Accepted: August 23, 2016
Published: August 23, 2016

Downloaded via LAWRENCE BERKELEY NATL LABORATORY on June 14, 2018 at 21:22:31 (UTC).
See https://pubs.acs.org/sharingguidelines for options on how to legitimately share published articles.

ACS Publications © 2016 American Chemical Society

DOI: 10.1021/acsami.6b06714
ACS Appl. Mater. Interfaces 2016, 8, 23696−23705

The impact of integrating catalysts and semiconductors is multifaceted,[14,15] with properties emerging from specific, difficult-to-predict materials interactions, which may change under operating conditions, as highlighted by recent work on adaptive junctions.[16−18] Generally applicable predictive models are not yet available, requiring discoveries to proceed via synthesis and measurement of new material combinations. Considerable effort has been devoted to interfacing oxygen evolution catalysts with $BiVO_4$ under near-neutral conditions.[4,19−32] With Co−Pi and FeOOH coatings, improved photoelectrochemical performance has been attributed to suppression of electron−hole recombination at the interface.[4,20,22] With respect to the PEC performance of integrated photoanodes, the specific character of the coating/semiconductor interface may be equally or more important than the electrocatalytic activity of the coating, as illustrated by the poor overall performance of IrO_x integrated with $BiVO_4$.[25,29] Choi and co-workers have also demonstrated that a dual coating of FeOOH, which improves interface quality, and NiOOH, which increases catalytic activity and affects Helmholtz layer formation, greatly enhances the performance of $BiVO_4$ photoelectrodes.[30]

Although most studies of $BiVO_4$/catalyst assemblies are performed under near-neutral conditions, operation under strongly acidic or basic conditions beneficially minimizes polarization losses and enables production of pure O_2 and H_2 product streams from water splitting devices.[33,34] However, the stability of $BiVO_4$ is poor under alkaline conditions, and longer operational lifetime can be obtained under near-neutral pH conditions.[35] In the present study we utilize a pH 13 electrolyte to balance material stability and system efficiency in a full water splitting device. Coating $BiVO_4$ with catalyst films can improve stability under alkaline conditions, as demonstrated with atomic layer deposited (ALD) CoO_x,[36] ALD TiO_2 films with sputtered Ni catalyst,[12] and a conformal coating of $ZnFe_2O_4$ on a nanoporous $BiVO_4$ photoanode.[37]

Identifying beneficial $BiVO_4$/catalyst interactions by investigating a range of catalyst compositions could significantly improve PEC performance and afford new insight into operable interfacial mechanisms. Motivated by high-throughput methods employed for energy materials and device discovery and optimization,[38−40] including catalysts and protective coatings on $BiVO_4$,[25,41] we pursued the integration of promising new Ce-rich pseudoquaternary oxide OER catalysts[42−45] with $BiVO_4$ using improved automated PEC characterization and advanced data processing to identify multifunctional catalyst/semiconductor interfaces.[13]

In our combinatorial study of 858 inkjet-printed (IJP) metal oxide coatings on thin film $BiVO_4$, we identify compositions that create $BiVO_4$-based photoanodes whose performance under alkaline conditions (pH 13) is much higher than anticipated from the optical and dark electrocatalytic properties of the metal oxides. The unexpectedly high photoanode performance is indicative of beneficial interfacial processes. Our earlier study of (Ni−La−Co−Ce)O_x catalyst libraries inkjet-printed on $BiVO_4$ revealed the following: (1) The optimal catalyst composition when integrated with $BiVO_4$ was shifted toward the (La+Ce)−rich compositions relative to the optimal electrocatalysts deposited onto fluorine-doped tin oxide (FTO). (2) The most active catalyst coatings were high-order compositions with 3 or 4 metal elements. (3) The photoanode performance was not strongly dependent upon catalyst loading, with the intermediate loading investigated yielding the highest performing photoanodes. In contrast, our current study of (Ni−Fe−Co−Ce)O_x reveals the following: (1) The optimal catalyst compositions when integrated with $BiVO_4$ are substantially different than those of the optimal electrocatalysts on FTO. (2) The optimal catalyst composition varies with catalyst loading. (3) The lowest loading achievable using the inkjet printing method produces the highest activity, indicating that additional improvements in activity may result from further optimization of composition and loading. (4) While interesting trends are observed in the high-order composition spaces, the optimal photoelectrochemical power conversion is obtained on the (Fe−Ce)O_x pseudobinary line and shifts toward Fe-rich compositions with decreasing loading.

Motivated by these observations from the high-throughput experiments, we performed additional experiments using traditional techniques, starting with a scaled-up photoanode with the optimal IJP $Fe_{0.5}Ce_{0.5}O_x$ catalyst. The performance of this scaled-up $Fe_{0.5}Ce_{0.5}O_x$ composition and loading exceeds that of the previously investigated $La_{0.2}Co_{0.2}Ce_{0.6}O_x$. Given the improvements in photoanode performance with decreased catalyst loading, we additionally employed a PED technique to prepare a $Fe_{0.5}Ce_{0.5}O_x$ catalyst composition, demonstrating that catalyst coatings on the order of 1 nm are sufficient to improve the performance of $BiVO_4$-based photoanodes.[27]

2. EXPERIMENTAL SECTION

2.1. Photoanode Library Design and Synthesis. The design and synthesis of libraries of photoanode assemblies, as well as the instrumentation, experimental methods, and analysis techniques for evaluating the libraries has been reported in detail previously.[13] In this work, we utilized these methods to investigate the (Ni−Fe−Co−Ce)O_x OER catalyst composition space as coatings on $BiVO_4$. In brief, a uniform $BiVO_4$ film was spin-coated onto a 100 cm^2 FTO-coated glass substrate (TEC 15, Sigma-Aldrich).[13,35,46] Discrete composition libraries of mixed-metal oxide coatings containing Ni, Fe, Co, and Ce were inkjet printed at 10 atom % composition steps onto the $BiVO_4$ film, as shown in Figure 1. The libraries were calcined in air at 350 °C

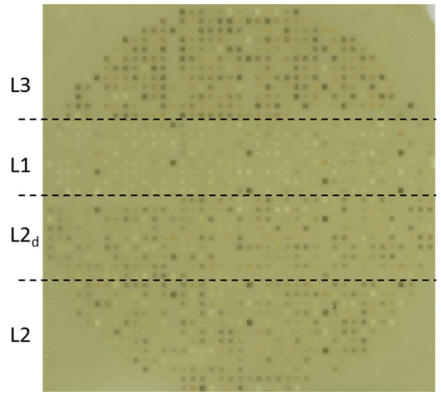

Figure 1. Photograph of the 10 cm × 10 cm FTO/glass plate with the (Ni−Fe−Co−Ce)O_x catalyst library on $BiVO_4$. The regions of the library containing catalyst loadings L1, L2, $L2_d$ (duplicate of the L2 loading library), and L3 are marked, with each of these regions containing the same 286 catalyst compositions.

to produce mixed-metal oxides with undetermined oxygen stoichiometry; thus, the samples are labeled using the intended cation composition. Our previous work has shown that the elemental oxide phases prepared by the inkjet printing and calcination method are NiO, Fe_2O_3, Co_3O_4, and CeO_2 and that mixed-metal oxide coatings may contain nanostructured phase mixtures, in particular mixtures of CeO_2 with (Ni,Fe,Co)O rock-salt alloys that exhibit atomically sharp

DOI: 10.1021/acsami.6b06714
ACS Appl. Mater. Interfaces 2016, 8, 23696−23705

grain boundaries. While interactions between mixed-metal oxides and $BiVO_4$ may lead to variation in the phase behavior and morphology from these previous variations, these properties are not characterized in the present work as the photoanode library samples are not amenable to nanocharacterization.[47]

Using 10 atom % intervals, the $(Ni–Fe–Co–Ce)O_x$ composition space contains 286 unique compositions, and the photoanode library shown in Figure 1 includes three different loadings for each composition: 0.75, 1.9, and 3.6 nmol mm^{-2}, labeled L1, L2 (and $L2_d$ for a duplicate copy of loading L2), and L3, respectively. This range of loadings corresponds to a nominal thickness range of 5–20 nm, but as detailed in previous work, each mixed-metal oxide coating is discontinuous and coarse on the 1 μm scale, producing substantial variations in coating thickness. The combined composition–thickness library contained 858 unique coatings on $BiVO_4$ that along with the 286 duplicate $L2_d$ samples comprise the "photoanode library" screened for photoelectrocatalysis of the oxygen evolution reaction. To prevent convolution of spatial and temporal variations with composition, the 286 compositions were randomly distributed within each block of loadings.

A duplicate composition-loading library of metal oxides was deposited directly onto a 100 cm^2 FTO-coated glass substrate to create the "catalyst library," which was used to measure the optical and OER electrocatalytic properties of the metal oxides in the absence of the $BiVO_4$ light absorber.

2.2. Photoelectrochemical Characterization. The optical and electrocatalytic properties of the catalyst library on FTO-glass were characterized at an OER overpotential of 350 mV in pH 13 electrolyte (0.1 M NaOH (aqueous) with 0.5 M Na_2SO_4 (aqueous) as supporting electrolyte), using methods similar to those previously reported.[13,48] The same custom scanning drop photoelectrochemical cell (SDC) was used to measure the photoelectrochemical response of the photoanode library by measurement of toggled-illumination cyclic voltammograms (CVs) for each photoanode assembly.[13,48] Given the 2 mm pitch between samples (1 mm of uncoated $BiVO_4$ on all sides of each 1 mm × 1 mm coating), independent PEC measurements were obtained by limiting the electrolyte contact diameter to be less than 3 mm and additionally employing a 1 mm diameter illumination footprint to confine the illumination to within the printed area of the respective sample. Over the spectral range of 390–600 nm (the portion of the spectrometer range with appreciable absorption from the $BiVO_4$ film), the broadband light source used has an irradiance approximately four times greater than that of 1 sun AM 1.5G.

3. RESULTS AND DISCUSSION

3.1. Performance of Integrated Photoanodes. The anodic sweep of each toggled-illumination CV was used to evaluate the photoelectrochemical performance of each assembly in the photoanode library, as illustrated in Figure 2a. The photocurrent density ($J_{photo}(V)$) was calculated as the difference between the illuminated and dark current density signals from the anodic sweep. As illustrated in Figure 2b, two primary photoanode performance metrics were extracted from the $J_{photo}(V)$ curve: (1) the photocurrent density at the Nernstian potential for the OER (J_{O_2/H_2O}) and (2) the maximum photoelectrochemical power conversion (P_{max}), as described previously.[13]

The photocurrent density curves from the best $(Ni–Fe–Co–Ce)O_x$-coated photoanode assemblies are compared to uncoated $BiVO_4$ in Figure 2c. The photocurrent density at the Nernstian potential of the applicable redox reaction is a common performance metric for photoelectrodes.[49] For each photoanode, we denote the photocurrent density at 1.23 V vs RHE (the Nernstian potential of the O_2/H_2O couple) as J_{O_2/H_2O}, and use this value as one figure of merit (FOM) to construct composition maps of photoanode performance. Two

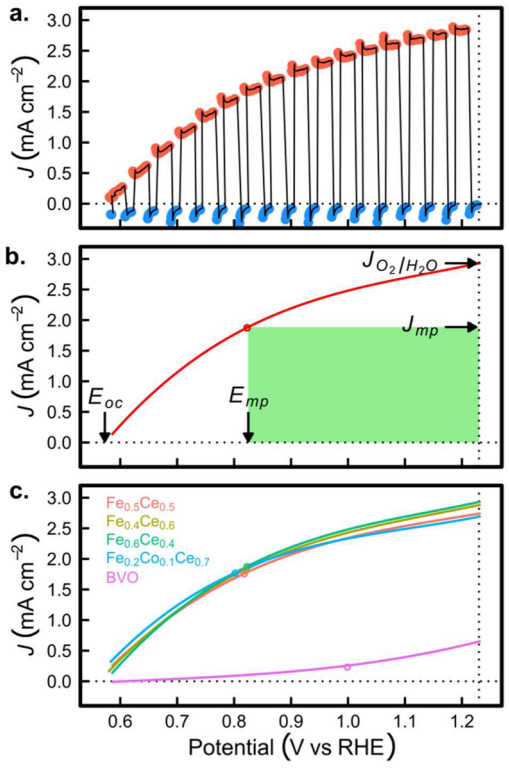

Figure 2. (a) Anodic sweep of the CV acquired on L1 sample $Fe_{60}Ce_{40}O_x$ with illuminated (1.34 s) and dark (0.67 s) intervals highlighted in red and blue, respectively. (b) Disregarding the current transients upon illumination toggling, the photocurrent density is fit to a third-order polynomial (red line), providing the $J_{photo}(V)$ signal from which performance metrics are calculated. The short circuit current density (J_{O_2/H_2O}) is labeled, together with the maximum power point (red circle), which corresponds to an electrochemical power generation of P_{max} (shaded green area). (c) Representative photocurrent density signals from 4 of the best photoanodes are shown along with the photocurrent density signal from bare $BiVO_4$. The maximum power point is circled for each photoanode.

different representations of the composition map of J_{O_2/H_2O} are shown for the L1 samples in Figure 3. Figure 3a shows the entire pseudoquaternary composition space using three connected sets of four pseudoternary triangles. The four large triangles are the four faces of the $(Ni–Fe–Co–Ce)O_x$ composition tetrahedron shown in Figure 3b, with each composition containing at most 3 metals. Considering these to be the outer shell of the tetrahedron, the inner shells are shown in Figure 3c,d, where each composition in these shells contains at least 10 and 20% of each metal, respectively. By unfolding the three shells of the tetrahedron, the flattened composition map of Figure 3a depicts the J_{O_2/H_2O} as a color scale for each of 286 compositions with L1 loading. The prime and double-prime element labels at the vertices of the inner composition triangles are defined in the figure caption and in Table S1.

The compositions in the $(Ni–Fe–Co–Ce)O_x$ composition space that yield the best photoanodes are between $Fe_{0.6}Ce_{0.4}O_x$ and $Fe_{0.4}Ce_{0.6}O_x$ with loading L1, as seen in Figure 3a. Local maxima are also found on the $(Ni–Ce)O_x$ and $(Co–Ce)O_x$ pseudobinary lines, with the three Ce-containing pseudobinary composition spaces producing higher J_{O_2/H_2O} values than the constituent single-metal oxides. The local maxima on the

DOI: 10.1021/acsami.6b06714
ACS Appl. Mater. Interfaces 2016, 8, 23696–23705

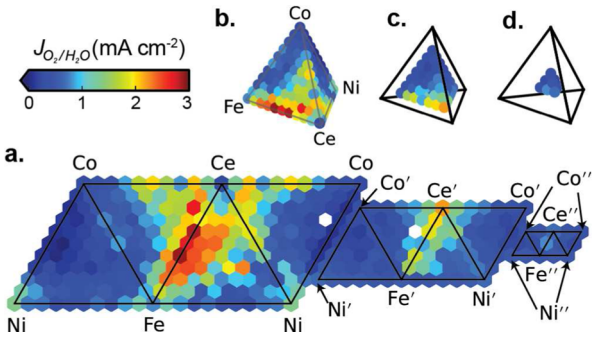

Figure 3. Composition map of J_{O_2/H_2O} for L1 samples. (a) The full pseudoquaternary composition space is shown as the flattened set of pseudoternary faces with the 3 sets of 4 faces containing the compositions from the 3 concentric shells of the tetrahedron composition plot. These 3 shells of compositions are shown in b–d, respectively, using the common false color scale. The end-member compositions of the 3 shells are labeled M, M′, and M″ (where M = Ni, Fe, Co, or Ce), respectively. Fe′ corresponds to $Ce_{0.1}Fe_{0.7}Ni_{0.1}Co_{0.1}O_x$; Fe" corresponds to $Ce_{0.2}Fe_{0.4}Ni_{0.2}Co_{0.2}O_x$. The definition of each composition label is provided in Table S1.

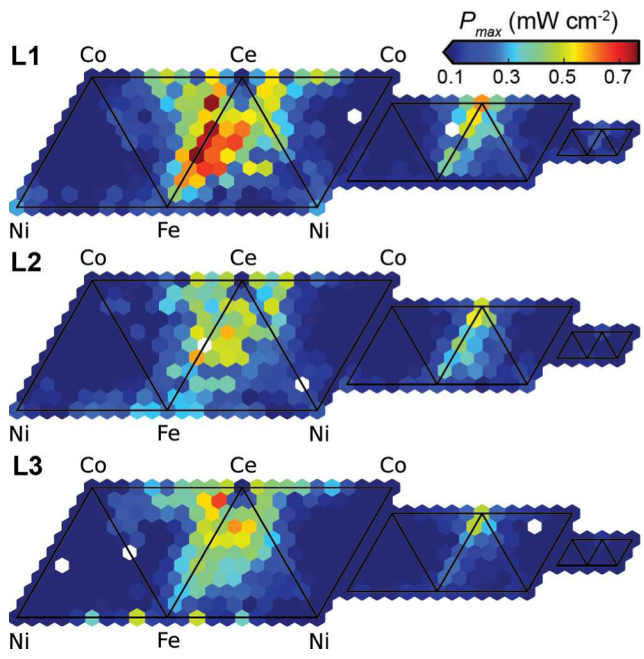

Figure 4. Composition maps of P_{max} for all three catalyst loadings, plotted with a common color scale using the flattened pseudoternary triangle scheme of Figure 3a.

pseudobinary lines extend into the pseudoternary spaces, with the best pseudoternary compositions obtained by adding Ni to $(Fe–Ce)O_x$ compositions. The local maxima of $J_{O_2}/_{H_2O}$ extends into the quaternary space around composition Ce′ ($Ni_{0.1}Fe_{0.1}Co_{0.1}Ce_{0.7}O_x$). The optimal performance in catalyst composition space depends significantly upon the catalyst loading, as seen in the composition maps of $J_{O_2}/_{H_2O}$ for all three catalyst loadings (see Figure S2). These observed trends are distinct from those previously reported for the $(Ni–La–Co–Ce)O_x$ catalyst libraries on $BiVO_4$, in which the optimal composition regions were the same at all three catalyst loadings and the best 3- and 4-metal catalysts far outperformed any 1- or 2-metal catalyst.[13]

An even more important FOM for photoanode assemblies is their ability to convert photon energy to electrochemical energy. Assuming 100% Faradaic efficiency, the electrochemical power generation (or power saved[49] compared to an ideal electrocatalyst operating at the Nernstian potential) is given by the product of the bias potential (with respect to the OER Nernstian potential) and the corresponding photocurrent, which is readily calculated from the data shown in Figure 2. For a photoanode, its maximum electrochemical power generation (P_{max}) is the single most meaningful scalar performance metric, as illustrated in Figure 2b.

The map of P_{max} is shown in Figure 4 as a function of composition and catalyst loading, revealing similar trends as those observed for $J_{O_2}/_{H_2O}$. At the highest coverage (L3), the best P_{max} performance is obtained with 60–90 metal atom % Ce, with the peak performances at the compositions $Ni_{0.1}Fe_{0.2}Ce_{0.7}O_x$, $Fe_{(0.1–0.2)}Co_{(0.1–0.2)}Ce_{(0.8–0.7)}O_x$, and $Ni_{0.1}Co_{0.1}Fe_{(0.1–0.2)}Ce_{(0.6–0.7)}O_x$. With decreasing catalyst coverage, these compositions retain approximately the same P_{max} performance. However, the P_{max} increases for the $Fe_{(0.6–0.4)}Ce_{(0.4–0.6)}O_x$ pseudobinary compositions and the neighboring Ni-containing compositions such that at L1 loading these are the most active compositions in the entire library. Photoanodes in the 99th percentile of P_{max} (above 0.64 mW cm^{-2}) are found only at L1 loadings close to the $Fe_{(0.6–0.4)}Ce_{(0.4–0.6)}O_x$ pseudobinary compositions. The global maximum of 0.76 mW cm^{-2} is obtained with the $Fe_{0.6}Ce_{0.4}O_x$-L1 sample and is approximately 13.6 times larger than the 0.056 mW cm^{-2} provided by bare $BiVO_4$ (measured on this library plate in a region without catalyst coating).

The P_{max} of bare $BiVO_4$ is in the 10th percentile of the photoanode library, meaning that approximately one tenth of the metal oxide coatings are deleterious to the PEC performance of $BiVO_4$. Mixed-metal oxide coatings typically do not significantly improve photoanode performance. In the present study, only 46 of 828 photoanode samples measured (less than 5.4%) exhibit P_{max} values in excess of 0.5 mW cm^{-2}, demonstrating that producing high-performance photoanodes requires specific catalyst compositions and loadings.

3.2. High-Throughput Screen of Photoanode Stability. Evaluation of PEC stability is particularly challenging for photoanodes as the target end-use involves pairing with a photocathode to determine the operational point in the $J_{photo}(V)$ curve, which will then vary due to the diurnal cycle. Ideally, the photoanode would be operated near its maximum power point, and to evaluate initial stability of the integrated photoanodes, we perform toggled-illumination chronoamperometry (CA) measurements at 0.8 V vs RHE (−0.43 V vs OER), which is near the potential of the maximum power point (E_{mp}) for the top-performing photoanodes in Figure 4. The photocurrent at P_{max} is sensitive to many degradation mechanisms because it is sensitive to changes in any of the common performance metrics: E_{OC}, $J_{O_2}/_{H_2O}$, and fill factor. The 86 compositions at the L2 loading producing the largest values of J_{photo} at 0.8 V vs RHE in the toggled-illumination CV scans were selected for stability evaluation from the original set of 256 compositions. CA measurements were performed on the duplicate L2 loading samples ($L2_d$) at 0.8 V vs RHE and the initial photocurrent densities shown in Figure 5a were determined after 4 s of toggled illumination, which allowed the settling of any initial, sharp transient currents. The final J_{photo} values, after 180 s of toggled illumination and CA measurement, are shown in Figure 5b. The highest-performing

DOI: 10.1021/acsami.6b06714
ACS Appl. Mater. Interfaces 2016, 8, 23696–23705

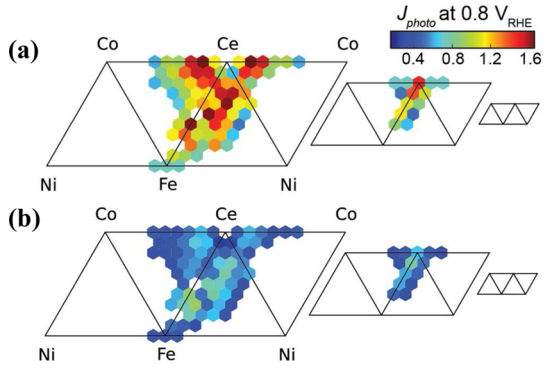

Figure 5. Composition maps of J_{photo} at 0.8 V vs RHE (−0.43 V vs O_2/H_2O) for catalyst library $L2_d$ (a) at t = 4 s toggled-illumination CA and (b) at t = 180 s toggled-illumination CA at 0.8 V vs RHE (−0.43 V vs O_2/H_2O).

photoanode compositions initially lie near the $(Fe-Ce)O_x$ pseudobinary line and extend into the pseudoternary spaces with addition of Ni or Co. After the 3 min illuminated stability test, the highest performing compositions remain near the $(Fe-Ce)O_x$ pseudobinary line, but J_{photo} has been lowered by up to 50% in some cases. Several compositions in the $(Ni-Fe-Ce)O_x$ pseudoternary composition space with 20 atom % Ni appear to be relatively more stable over this duration, indicating that incorporation of Ni into the $(Fe-Ce)O_x$ coatings is detrimental to initial PEC performance but enhances PEC stability.

To explore possible modes of degradation, a 30 min chopped-illumination CA experiment at 0.8 V vs RHE was performed on the $Fe_{0.6}Ce_{0.4}O_x$-L1 sample. The photocurrent signal as well as X-ray fluorescence characterization data are shown in Figure S8, revealing that the high-throughput CV and 30 min of CA resulted in losses of approximately 20% of the Bi and 50% of the V from the as-prepared photoanode. Due to the low loading of Ce and Fe, fluorescence signals overlapping with the Ce signal and the presence of Fe impurities in the glass substrate, these elements are not readily quantifiable; however, no loss of Ce or Fe is evident, in agreement with the established stability of CeO_2 and Fe_2O_3 under the electrochemical conditions. The loss of Bi and V suggests the primary degradation mechanism is (photo)corrosion of $BiVO_4$ with preferential loss of V, which is enabled by the direct electrolyte contact afforded by the discontinuous catalyst coating and in agreement with recent studies of $BiVO_4$ corrosion.[35] While these results motivate further exploration of conformal $(Ni-Fe-Ce)O_x$ protective coatings, we turn to additional analysis of the metal oxide libraries to identify the interfaces that yield the best PEC performance.

3.3. Data-Driven Identification of Optimal Interfaces.

Coating compositions that exhibit beneficial interactions with the light absorber can be identified through analysis of the combinatorial screening data. The formation of an optimal interface leads to PEC performance exceeding that expected given the independent properties of the light absorber and the metal oxide coating. Such emergent properties from catalyst/light absorber combinations are of particular interest for achieving peak performance in scaled and integrated systems, as well as for identifying interfacial properties that give rise to unexpected behavior and establishing rational approaches to interface engineering. By combining the PEC properties measured on the photoanode library with the optical and electrocatalytic properties of the catalyst library, we establish a model for evaluating the relative photoelectrochemical performance enhancement due to the catalyst/light absorber interface.

The OER catalytic current density (J_{cat}) was mapped over the catalyst library at a moderate OER overpotential of η = 0.35 V, an electrochemical potential that serves as a proxy for the (unknown) operational surface potential of the $BiVO_4$. Electrochromic transition metal oxide films become darker in alkaline electrolytes under OER operational conditions, due to oxidation of the catalyst,[48,50] motivating the use of *in situ* optical characterization to measure optical transmission and catalytic activity simultaneously after 25 s of polarization. The optical transmission efficiency ($\alpha_{T,cat}$, see Experimental Section) was calculated as the fraction of the transmitted photons over 390–600 nm (the primary $BiVO_4$ absorption range), as previously described in greater detail.[48]

We previously reported the OER catalytic activity in pH 14 electrolyte,[44] revealing similar activity in the $Ni_{0.25}Co_{0.25}Ce_{0.5}O_x$ and $Ni_{0.6}Fe_{0.4}O_x$ composition regions. In pH 13 electrolyte, as used in the present study, the best electrocatalytic activity is found in the $(Ni-Fe-Co)O_x$ pseudoternary composition space and is more Ni-rich with $Ni_{0.7}Co_{0.1}Fe_{0.2}O_x$ being the optimal catalyst (see Figure S5). None of these composition regions exhibit particularly high P_{max} values in the photoanode library. For all three loadings of the $(Ni-Fe-Co-Ce)O_x$ compositions, Figure 6 shows J_{cat} relative to $\alpha_{T,cat}$, with the color of the

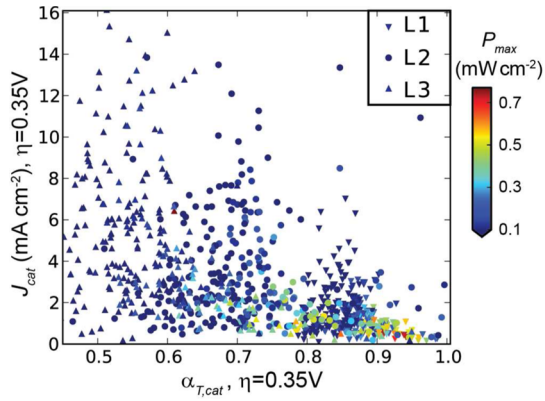

Figure 6. Each of the 858 library samples is plotted according to the optical transmission efficiency ($\alpha_{T,cat}$) and catalytic activity (J_{cat}) measured on the FTO/glass-supported library. Each sample is colored by the P_{max} measured on the $BiVO_4$ photoanode library. Each sample with high P_{max} (green to red colors) is surrounded by samples with much lower P_{max}, demonstrating the lack of a systematic relationship among $\alpha_{T,cat}$, J_{cat}, and P_{max}.

data points corresponding to the P_{max} value from the photoanode library sample with the equivalent metal oxide coating. One may expect the performance of the integrated photoanodes (P_{max}) to vary systematically with $\alpha_{T,cat}$ and J_{cat}, the operational optical transparency and catalytic activity of the catalyst coating. However, low-P_{max} data points are intermixed with high-P_{max} data points in Figure 6; thus, $\alpha_{T,cat}$ and J_{cat} of the dark electrocatalyst cannot alone robustly predict the behavior of integrated photoanodes. Indeed, these high-throughput results demonstrate that the complex composition-dependent interactions of the catalyst with the $BiVO_4$ light absorber strongly affect the photoanode performance.

DOI: 10.1021/acsami.6b06714
ACS Appl. Mater. Interfaces 2016, 8, 23696–23705

By applying a simple model for comparing P_{max} to $\alpha_{T,cat}$ and J_{cat}, the extent to which catalyst compositions over- or underperform expectations can be quantified. Following the model used in previous work,[45,48] we estimate a maximum relevant catalytic current density (J_{max} = 3 mA cm^{-2}), which is approximately equal to the maximum J_{O_2/H_2O} photocurrent density in Figure 3 and is approximately the maximum photocurrent that can be produced by the $BiVO_4$ film with the illumination source used to characterize the photoanode library. Any catalyst able to support a current density in excess of the J_{max} capable of being generated by the $BiVO_4$ light absorber is treated as having the same "activity" in our simple predictive model. The combined optical−catalytic efficiency ($\alpha_{C,cat}$, eq 1) is calculated as the product of the optical transmission efficiency and catalytic current efficiency:

$$\alpha_{C,cat} = \alpha_{T,cat}(\min[J_{cat}, J_{max}]/J_{max}) \quad (1)$$

The quantity $\alpha_{C,cat}$ serves as a dimensionless predictor of the relative performance of each integrated photoanode based on properties of the metal oxide coating. The composition maps of J_{cat}, $\alpha_{T,cat}$, and $\alpha_{C,cat}$ are shown in Figures S5−S8 for all three catalyst loadings and for the L1 samples in Figure 7a−c. More

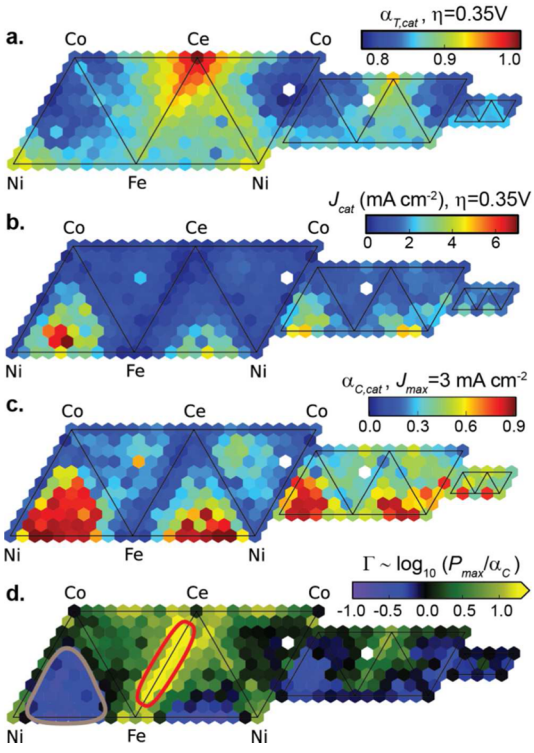

Figure 7. Composition maps of (a) optical transmission efficiency ($\alpha_{T,cat}$), (b) catalytic current density (J_{cat}), and (c) the ensuing combined figure of merit ($\alpha_{C,cat}$) for the L1 catalyst samples from the FTO/glass-supported library. The parameter Γ compares photoanode performance (P_{max}) to that predicted by $\alpha_{C,cat}$, and the corresponding composition map is shown in d.

sophisticated models would be required to predict absolute J−E characteristics of photoanodes,[50] but eq 1 facilitates quantifying the relative predicted performance, which is sufficient for the present study.

The experimentally measured performance for each photoanode library sample can be compared to this calculated combined optical−catalytic efficiency from the corresponding catalyst library sample to identify which catalyst compositions perform well-above or well-below this expectation. We make this comparison using the quantities

$$\Gamma' = \log_{10}(P_{max}/\alpha_{C,cat}) \quad (2)$$

$$\Gamma = \Gamma' - \text{median}(\Gamma') \quad (3)$$

The parameter Γ (eq 3) provides a log-scale quantification of the ratio of experimental photoanode performance to the predicted performance with a median shift so that values near 0 correspond to integrated performance comparable to that expected. The compositional maps of Γ are shown in Figure 7d for the L1 loading and in Figure S7 for all three catalyst loadings. In Figure 7d many compositions, highlighted with the tan circles, in the (Ni−Fe−Co)O_x space have one-tenth the anticipated performance (corresponding to Γ values approaching −1), which is indicative of deleterious effects upon integration onto $BiVO_4$. The compositions circled in red perform more than 10 times better than expected and lie primarily along the (Fe−Ce)O_x and (Co−Ce)O_x pseudobinary lines.

It is worth noting that the Γ values for CeO_x and FeO_x are approximately 0 and 0.7, respectively, indicating that the pure CeO_x coating behaves as expected and that FeO_x exhibits beneficial interactions with $BiVO_4$, as previously observed.[30] The Γ values for all 2-metal (Fe−Ce)O_x compositions are 1−1.5, indicating that the combination of both Fe and Ce into the metal oxide coating further improves the interface to $BiVO_4$. Indeed, these (Fe−Ce)O_x compositions are neither the most transparent nor the most active electrocatalysts but exhibit the best photoanode performance upon integration with $BiVO_4$.

The mixing of Ce and Fe oxides is markedly different from previously employed strategies for photoanode optimization. While the majority of the studies of catalyst/$BiVO_4$ assemblies are performed at near-neutral conditions, for example, Choi et al.[30] employed a bilayer coating in which NiO_x was added to FeOOH-coated $BiVO_4$ to enhance catalytic activity, there exist few reports of catalyst integration for alkaline conditions. For this application, bilayer coatings of an atomic layer deposited thin TiO_2 film followed by a sputtered Ni layer increased the stability of bismuth vanadate at pH 13 up to 4 h.[12] However, the onset potential was affected due to the interference of the protection layer with the $BiVO_4$/electrolyte junction energetics. Thinner catalyst CoO_x layers provide an improved onset potential in pH 13 without increasing the long-term stability of this light absorber.[36] The addition of CeO_x to FeO_x might be counterintuitive, given the relatively poor catalytic activity of CeO_x. This is reflected in Γ values that motivate future study of the (Fe−Ce)O_x/$BiVO_4$ interface and validation of the high-throughput discovery using traditional PEC techniques and alternative coating-synthesis techniques.

3.4. Validation Using Traditional Techniques. To validate the high-throughput results, we resynthesized the $Fe_{0.5}Ce_{0.5}O_x$-L1 sample by inkjet printing with a scaled-up area of approximately 1 cm^2 (compared to the 0.01 cm^2 sample size in the library). The cm^2 scale electrode is appropriate for characterization using a traditional PEC cell coupled to a calibrated AM 1.5G light source. CVs were acquired using the 1 cm^2 electrodes with and without illumination for catalyst-coated and bare $BiVO_4$ photoanodes in 0.1 M NaOH (pH 13) electrolyte, a standard technique for evaluating $BiVO_4$-based photoanodes under alkaline conditions.[12,36] The results are shown in Figure 8a and are compared to those of the uncoated

DOI: 10.1021/acsami.6b06714
ACS Appl. Mater. Interfaces 2016, 8, 23696−23705

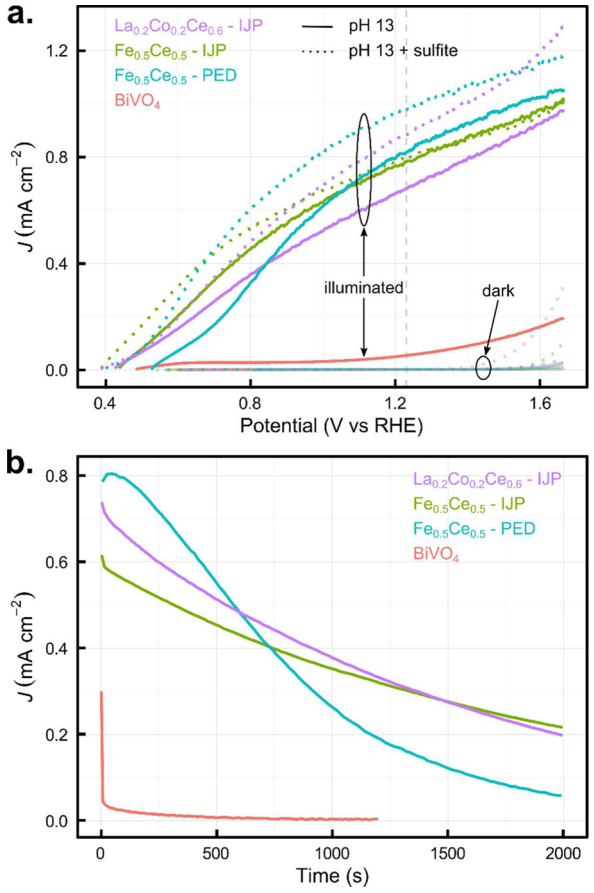

Figure 8. (a) Anodic sweep from 16 CV measurements in pH 13 electrolyte, using a traditional cell and AM 1.5G 1 sun light source. The illuminated (labeled) and dark (labeled) current density are shown for bare $BiVO_4$ and for the scaled-up IJP $Fe_{0.5}Ce_{0.5}O_x$-L1, PED $Fe_{0.5}Ce_{0.5}O_x$, and IJP $La_{0.2}Co_{0.2}Ce_{0.6}O_x$-L2 samples; the samples were measured without (solid lines) and then with the addition of 0.1 M sulfite (Na_2SO_3) (dashed lines) to the 0.1 M NaOH electrolyte. (b) Stability of the short circuit photocurrent density (1.23 V vs RHE) of bare $BiVO_4$ and scaled-up IJP $Fe_{0.5}Ce_{0.5}O_x$-L1, IJP $La_{0.2}Co_{0.2}Ce_{0.6}O_x$-L2, and PED $Fe_{0.5}Ce_{0.5}O_x$ are measured in 0.1 M NaOH under AM 1.5G 1 sun illumination.

$BiVO_4$ film and the scaled-up, previously reported photoanode containing the optimal coating from a (Ni−La−Co−Ce)O_x library.[13] These photocurrent−potential curves confirm that the $Fe_{0.5}Ce_{0.5}O_x$-L1 coating substantially improves the PEC performance. The integrated photoanode provides a photocurrent of 0.78 mA cm^{-2} and an onset potential of approximately 0.43 V vs RHE, rivalling the best values reported in pH 13[36] and may be further improved by optimizing deposition conditions.

To further evaluate the efficacy of the $Fe_{0.5}Ce_{0.5}O_x$-L1 coating, we compare the performance to previously reported coatings for $BiVO_4$-based photoanodes operating at pH 13. By considering the enhancement in photocurrent with respect to bare $BiVO_4$ at the OER Nernstian potential (1.23 V vs RHE), the influence of the coating is readily quantified independent of the base performance of the $BiVO_4$ light absorber, which varies substantially among the relevant works. The 14-fold enhancement demonstrated in Figure 8b is larger than both the 7-fold enhancement obtained with ALD CoO_x coatings and the 3-fold enhancement obtained with conformal $ZnFe_2O_4$ coatings. While those previously reported photoanodes exhibited slightly higher absolute current densities, the relative enhancement factor exhibited by (Fe−Ce)O_x demonstrates its capacity to yield top-performing photoanodes when integrated with optimized $BiVO_4$.

The shape of the CV under AM 1.5 illumination (Figure 8a) is similar to the photocurrent density curves from the high-throughput chopped-illumination CVs (Figure 2c). The greater value of the J_{O_2/H_2O} in the high-throughput experiments (2.74 mA cm^{-2}) relative to this traditional measurement (0.78 mA cm^{-2}) is consistent with the greater $BiVO_4$-absorbable photon flux in the library measurement than in the AM 1.5 spectrum.

To further investigate the photocatalytic performance of $Fe_{0.5}Ce_{0.5}O_x$-L1 on $BiVO_4$, the PEC oxidation of 0.1 M sulfite (Na_2SO_3, a sacrificial hole-acceptor exhibiting facile oxidation kinetics) in pH 13 electrolyte was compared to the OER experiments. Under illumination, the difference in E_{OC} between the sulfite-containing and sulfite-free experiments is small for the IJP catalyst-coated samples. Notably, this comparison provides information on the charge extraction efficiency of the catalyst and reveals a surprisingly similar photocurrent at anodic potentials. Indeed, despite the presence of reduced surface recombination rate at more cathodic potentials, the catalytic activity and the $BiVO_4$/catalyst interface generated by this composition is close to ideal. For $BiVO_4$, a light absorber with a fairly deep valence band and photogenerated holes are understood to be sufficiently energetic to perform the OER without an optimized electrocatalyst. However, $BiVO_4$ suffers substantially from high surface recombination rates, which can be alleviated through appropriate interface engineering. The high-throughput chopped-illumination CVs (see Figure 2a) provide additional evidence that the best catalyst/$BiVO_4$ assemblies exhibit reduced recombination rates compared to bare $BiVO_4$. The current transients upon illumination toggling, which are indicative of capacitive charging of surface states, are very low compared to bare $BiVO_4$ surfaces.

This characterization of the scaled-up photoanode provides a robust validation of the high-throughput result. The PEC stability of the $Fe_{0.5}Ce_{0.5}O_x$-L1 photoanode was investigated using an illuminated CA experiment at 1.23 V vs RHE under AM 1.5 illumination for 2000 s. The stability results for the scaled-up IJP catalyst-coated-$BiVO_4$ and bare $BiVO_4$ photoanodes are shown in Figure 8b. The photocurrent density of the $Fe_{0.5}Ce_{0.5}O_x$-L1 photoanode exceeds that of bare $BiVO_4$ by a factor of approximately 15 after 15 s, in agreement with the CVs acquired under illumination (Figure 8a), and increases to a value 60 times greater at 500 s. Despite the significantly increased photocurrent density of the coated $BiVO_4$ compared to the uncoated $BiVO_4$ film after 30 min, further improvements in stability will be required to approach practical photoanode lifetimes.

3.5. Photoelectrodeposited Coatings. Photoelectrodeposition (PED) is an attractive deposition method for photoanode coatings that is complementary to IJP in that thermal calcination is not required and thinner, more conformal coatings can be synthesized.[17,51] To ascertain if the thin $Fe_{0.5}Ce_{0.5}O_x$ coatings performed well using this alternative deposition method, PED was carried out in an undivided cell under simulated AM1.5G 1 sun illumination in an equimolar solution of 50 mM Fe(III) and 50 mM Ce(III) precursors as the electrolyte, using a Ag/AgCl reference electrode, a Pt mesh as counter electrode, and $BiVO_4$/FTO-glass as working electrode. XPS measurements (see Figure S8) of replicate

DOI: 10.1021/acsami.6b06714
ACS Appl. Mater. Interfaces 2016, 8, 23696−23705

samples confirm that the deposited catalyst has a stoichiometry of approximately $Fe_{0.5}Ce_{0.5}O_x$.

As seen in Figure 8a, the overall $J-E$ performance of the PED $Fe_{0.5}Ce_{0.5}O_x$ catalyst was similar to that of the IJP catalysts but with higher J_{sc} and more anodic onset potential. The higher saturation photocurrent density is suggestive of increased light transparency for the PED catalyst, in agreement with a lower, controlled loading obtained with this technique,[27] whereas the better fill factor of the PED sample highlights the presence of higher series resistance in the IJP sample. This finding is in agreement with a thinner layer obtained by PED, which provides a less resistive Ce-containing coating. However, the more anodic onset potential may be due to different energetics between the different semiconductor/catalyst interfaces of the IJP and PED samples. This interface plays a fundamental role in the separation and collection of photogenerated charge carriers and ultimately affects surface recombination.[17] Specifically, the PED $Fe_{0.5}Ce_{0.5}O_x$ sample shows more pronounced surface recombination, as the CV curve clearly exhibits a shallower slope close to the onset potential and an inflection point with improved charge extraction at increasingly anodic potentials. Although one can conclude that the IJP catalyst more efficiently passivates $BiVO_4$ surface states, with a consequent improvement in the onset potential and steeper onset of photocurrent, the source of the surface recombination of the nonoptimized catalyst deposited by the PED method may arise from multiple sources. Indeed, nonideal catalytic activity is also revealed by the comparison of the $Fe_{0.5}Ce_{0.5}O_x$ PED coating, with and without sacrificial reagent; without the sacrificial reagent, the anodic sweep of the PED sample shows more anodic onset potential and lower photocurrent than in the presence of sacrificial reagent.

In addition to verifying the high-throughput identification of the $Fe_{0.5}Ce_{0.5}O_x$ coating, the demonstration of excellent photoelectrochemical performance using PED provides opportunities for further coating optimization. Coating deposition via PED[52,53] preserves the integrity of the semiconductor by preventing its reduction to an inactive phase and inherently places catalysts at the locations where the photogenerated holes are most readily available for solar water oxidation.[54,55] Moreover, the solution-based nature of PED facilitates deposition of ion-permeable (oxy)hydroxide or hydrous oxide catalysts, yielding "adaptive" junctions that may provide larger photovoltages for solar water oxidation.[16−18] The PED $Fe_{0.5}Ce_{0.5}O_x$ coating provides little parasitic light absorption to the thin, approximately 1 nm coating of the highly transparent metal oxide, and the demonstrated catalytic limitation of the PED coating motivates integration of an additional OER cocatalyst to further optimize photoanode performance.

As seen in Figure 8b, the PEC stability of the PED $Fe_{0.5}Ce_{0.5}O_x$ coating was measured using an illuminated CA experiment at 1.23 V vs RHE under AM 1.5 illumination for 2000 s. Consistent with this PED coating being thinner and more transparent than the IJP-deposited coating, the photocurrent density is initially greater but decays more quickly with time than do the IJP-deposited coatings. To identify the underlying cause for degradation in photocurrent, both as-synthesized and post-PEC testing photoanodes were characterized by XPS. This analysis indicates preferential loss of V at the surface, with an associated apparent enrichment of Bi (Table S2). This data is consistent with recent work on the chemical and photochemical instability of $BiVO_4$ films.[35] Therefore, we surmise that the observed instability of the coated photoanodes is caused by the dissolution of the $BiVO_4$ film initiated at locations relatively unprotected by the discontinuous IJP coating and potentially discontinuous PED-deposited coating. Future investigation of the spatial inhomogeneity of dissolution and differences as a function of coating deposition method are anticipated to provide clues for further enhancing stability.

4. CONCLUSIONS

Automated photoelectrochemistry was used for the high-throughput evaluation of 858 discrete solar fuels photoanode assemblies with a uniform $BiVO_4$ light absorber and a library of coatings that included the entire $(Ni-Fe-Co-Ce)O_x$ composition space and three different loadings. This combinatorial study identified the $(Fe-Ce)O_x$ pseudobinary as containing compositions providing unanticipated high-performance coatings that greatly enhanced the OER photoelectrocatalytic activity of $BiVO_4$. This discovery was verified using traditional characterization of a scaled-up, inkjet-printed $Fe_{0.5}Ce_{0.5}O_x/BiVO_4$ electrode that produced a photovoltage of 0.8 V (E_{OC} = 0.43 V vs RHE) under AM 1.5 illumination, which is in the top tier of thin film $BiVO_4$ photoanodes under alkaline conditions. The efficacy of this surface oxide coating composition was substantiated by PEC characterization of photoanode assemblies prepared by photoanodic electrochemical deposition of $Fe_{0.5}Ce_{0.5}O_x$ onto $BiVO_4$, with lower loading providing increased photocurrent density J_{O_2/H_2O}. These results point to the unanticipated beneficial role of CeO_x on mitigating the surface recombination caused by surface/interfacial defects on $BiVO_4$, which will be the subject of future investigations. We anticipate that the findings presented here could also be incorporated into the design of high efficiency systems that utilize state-of-the-art approaches to doping, nanostructuring, and heterostructuring of $BiVO_4$.

■ ASSOCIATED CONTENT

Supporting Information

The Supporting Information is available free of charge on the ACS Publications website at DOI: 10.1021/acsami.6b06714.

Experimental details, data processing details, data analyses, and additional figure of merit composition maps at additional catalyst loadings (PDF)

■ AUTHOR INFORMATION

Corresponding Authors

*E-mail: fmtoma@lbl.gov.
*E-mail: gregoire@caltech.edu.
*E-mail: jahaber@caltech.edu.

Author Contributions

A.S. and D.G. contributed equally to this work.

Notes

The authors declare no competing financial interest.

■ ACKNOWLEDGMENTS

This material is based upon work performed by the Joint Center for Artificial Photosynthesis, a DOE Energy Innovation Hub, supported through the Office of Science of the U.S. Department of Energy (Award No. DE-SC0004993).

DOI: 10.1021/acsami.6b06714
ACS Appl. Mater. Interfaces 2016, 8, 23696−23705

ABBREVIATIONS

$A_{BVO}(\lambda)$, Fractional absorption spectrum of the $BiVO_4$ thin film
CA, Chronoamperometry
CV, Cyclic voltammetry (or cyclic voltammogram)
$E_{AM1.5}(\lambda)$, Spectral irradiance of global air mass 1.5 (ASTM 6173-03)
$E_{lamp}(\lambda)$, Spectral irradiance of the light source used in the high-throughput measurements
E_{OC}, Open circuit potential for a photoanode under illumination
E_{mp}, Potential at the maximum power point
J_{cat}, Oxygen evolution reaction current density of an electrocatalyst at 1.58 V vs RHE (0.35 V vs O_2/H_2O)
J_{mp}, Photocurrent density at the maximum power point of a photoanode
J_{O_2/H_2O}, Photocurrent density of a photoanode measured at the Nernstian potential for the oxygen evolution reaction
J_{max}, Maximum relevant electrocatalytic current density for the $BiVO_4$ thin film; defined for the evaluation and prediction of catalyst performance upon integration into a photoanode
$J_{photo}(V)$, Photocurrent density calculated from the high-throughput, toggled-illumination CVs
$N_{lamp}(\lambda)$, Photon flux of the light source used in the high-throughput measurements
P_{max}, Maximum electrochemical power generation from $J_{photo}(V)$ of a photoanode, which demarcates the maximum power point
$T(\lambda)$, Fractional optical transmission spectrum of a photoanode or electrocatalyst
$T_{cat}(\lambda)$, Fractional optical transmission spectrum of an electrocatalyst sample
α_{cat}, Combined optical−electrocatalytic efficiency of an electrocatalyst used in the evaluation and prediction of performance upon integration into a photoanode
$\alpha_{T,cat}$, Optical transmission efficiency of an electrocatalyst measured *in situ* at 1.58 V vs RHE; calculated as the fractional transmission of photons that are expected to be absorbed by the light absorber, which is particular to the specific lamp spectrum and thin film $BiVO_4$ of the present work
η_{OER}, Overpotential for the OER; potential applied to a catalyst with respect to the O_2/H_2O Nernstian potential
Γ', Photoanode performance compared to that predicted from the optical and electrical performance of the isolated catalysts; calculated as the log-ratio of the maximum electrochemical power generation of the photoanode and the combined optical−electrocatalytic efficiency of the catalyst
Γ, Relative photoanode performance compared to that predicted from the isolated catalysts; akin to Γ' but shifted so that the median value for the photoanode library is 0

REFERENCES

(1) Walter, M. G.; Warren, E. L.; McKone, J. R.; Boettcher, S. W.; Mi, Q.; Santori, E. A.; Lewis, N. S. Solar Water Splitting Cells. *Chem. Rev.* **2010**, *110*, 6446−6473.

(2) McCrory, C. C. L.; Jung, S.; Ferrer, I. M.; Chatman, S. M.; Peters, J. C.; Jaramillo, T. F. Benchmarking Hydrogen Evolving Reaction and Oxygen Evolving Reaction Electrocatalysts for Solar Water Splitting Devices. *J. Am. Chem. Soc.* **2015**, *137*, 4347−4357.

(3) McCrory, C. C. L.; Jung, S.; Peters, J. C.; Jaramillo, T. F. Benchmarking Heterogeneous Electrocatalysts for the Oxygen Evolution Reaction. *J. Am. Chem. Soc.* **2013**, *135*, 16977−16987.

(4) Abdi, F. F.; Han, L.; Smets, A. H. M.; Zeman, M.; Dam, B.; van de Krol, R. Efficient solar water splitting by enhanced charge separation in a bismuth vanadate-silicon tandem photoelectrode. *Nat. Commun.* **2013**, *4*, 2195.

(5) Bornoz, P.; Abdi, F. F.; Tilley, S. D.; Dam, B.; van de Krol, R.; Graetzel, M.; Sivula, K. A Bismuth Vanadate−Cuprous Oxide Tandem Cell for Overall Solar Water Splitting. *J. Phys. Chem. C* **2014**, *118*, 16959−16966.

(6) Han, L.; Abdi, F. F.; Perez Rodriguez, P.; Dam, B.; van de Krol, R.; Zeman, M.; Smets, A. H. M. Optimization of amorphous silicon double junction solar cells for an efficient photoelectrochemical water splitting device based on a bismuth vanadate photoanode. *Phys. Chem. Chem. Phys.* **2014**, *16*, 4220−4229.

(7) Han, L.; Abdi, F. F.; van de Krol, R.; Liu, R.; Huang, Z.; Lewerenz, H.-J.; Dam, B.; Zeman, M.; Smets, A. H. M. Efficient Water-Splitting Device Based on a Bismuth Vanadate Photoanode and Thin-Film Silicon Solar Cells. *ChemSusChem* **2014**, *7*, 2832−2838.

(8) Cooper, J. K.; Gul, S.; Toma, F. M.; Chen, L.; Glans, P.-A.; Guo, J.; Ager, J. W.; Yano, J.; Sharp, I. D. Electronic Structure of Monoclinic BiVO4. *Chem. Mater.* **2014**, *26*, 5365−5373.

(9) Cooper, J. K.; Gul, S.; Toma, F. M.; Chen, L.; Liu, Y.-S.; Guo, J.; Ager, J. W.; Yano, J.; Sharp, I. D. Indirect Bandgap and Optical Properties of Monoclinic Bismuth Vanadate. *J. Phys. Chem. C* **2015**, *119*, 2969−2974.

(10) Park, Y.; Kang, D.; Choi, K.-S. Marked enhancement in electron-hole separation achieved in the low bias region using electrochemically prepared Mo-doped BiVO4 photoanodes. *Phys. Chem. Chem. Phys.* **2014**, *16*, 1238−1246.

(11) Ding, C.; Shi, J.; Wang, D.; Wang, Z.; Wang, N.; Liu, G.; Xiong, F.; Li, C. Visible light driven overall water splitting using cocatalyst/BiVO4 photoanode with minimized bias. *Phys. Chem. Chem. Phys.* **2013**, *15*, 4589−4595.

(12) McDowell, M. T.; Lichterman, M. F.; Spurgeon, J. M.; Hu, S.; Sharp, I. D.; Brunschwig, B. S.; Lewis, N. S. Improved Stability of Polycrystalline Bismuth Vanadate Photoanodes by Use of Dual-Layer Thin TiO2/Ni Coatings. *J. Phys. Chem. C* **2014**, *118*, 19618−19624.

(13) Guevarra, D.; Shinde, A.; Suram, S. K.; Sharp, I. D.; Toma, F.; Haber, J. A.; Gregoire, J. Development of solar fuels photoanodes through combinatorial integration of Ni-La-Co-Ce oxide catalysts on BiVO4. *Energy Environ. Sci.* **2016**, *9*, 565−580.

(14) Hu, S.; Lewis, N. S.; Ager, J. W.; Yang, J.; McKone, J. R.; Strandwitz, N. C. Thin-Film Materials for the Protection of Semiconducting Photoelectrodes in Solar-Fuels Generators. *J. Phys. Chem. C* **2015**, *119*, 24201−24228.

(15) Smith, W. A.; Sharp, I. D.; Strandwitz, N. C.; Bisquert, J. Interfacial band-edge energetics for solar fuels production. *Energy Environ. Sci.* **2015**, *8*, 2851−2862.

(16) Lin, F.; Boettcher, S. W. Adaptive semiconductor/electrocatalyst junctions in water-splitting photoanodes. *Nat. Mater.* **2013**, *13*, 81−86.

(17) Lin, F.; Bachman, B. F.; Boettcher, S. W. Impact of Electrocatalyst Activity and Ion Permeability on Water-Splitting Photoanodes. *J. Phys. Chem. Lett.* **2015**, *6*, 2427−2433.

(18) Nellist, M. R.; Laskowski, F. A. L.; Lin, F.; Mills, T. J.; Boettcher, S. W. Semiconductor−Electrocatalyst Interfaces: Theory, Experiment, and Applications in Photoelectrochemical Water Splitting. *Acc. Chem. Res.* **2016**, *49*, 733−740.

(19) Wang, D. E.; Li, R. G.; Zhu, J.; Shi, J. Y.; Han, J. F.; Zong, X.; Li, C. Photocatalytic Water Oxidation on BiVO4 with the Electrocatalyst as an Oxidation Cocatalyst: Essential Relations between Electrocatalyst and Photocatalyst. *J. Phys. Chem. C* **2012**, *116*, 5082−5089.

(20) Abdi, F. F.; van de Krol, R. Nature and Light Dependence of Bulk Recombination in Co-Pi-Catalyzed BiVO4 Photoanodes. *J. Phys. Chem. C* **2012**, *116*, 9398−9404.

(21) Wang, D.; Li, R.; Zhu, J.; Shi, J.; Han, J.; Zong, X.; Li, C. Photocatalytic Water Oxidation on BiVO4 with the Electrocatalyst as

DOI: 10.1021/acsami.6b06714
ACS Appl. Mater. Interfaces 2016, 8, 23696−23705

an Oxidation Cocatalyst: Essential Relations between Electrocatalyst and Photocatalyst. *J. Phys. Chem. C* **2012**, *116*, 5082−5089.
(22) Zhong, D. K.; Choi, S.; Gamelin, D. R. Near-Complete Suppression of Surface Recombination in Solar Photoelectrolysis by "Co-Pi" Catalyst-Modified W:BiVO4. *J. Am. Chem. Soc.* **2011**, *133*, 18370−18377.
(23) Jeon, T. H.; Choi, W.; Park, H. Cobalt-phosphate complexes catalyze the photoelectrochemical water oxidation of BiVO4 electrodes. *Phys. Chem. Chem. Phys.* **2011**, *13*, 21392−21401.
(24) Zhou, M.; Bao, J.; Bi, W.; Zeng, Y.; Zhu, R.; Tao, M.; Xie, Y. Efficient Water Splitting via a Heteroepitaxial BiVO4 Photoelectrode Decorated with Co-Pi Catalysts. *ChemSusChem* **2012**, *5*, 1420−1425.
(25) Ye, H.; Park, H. S.; Bard, A. J. Screening of Electrocatalysts for Photoelectrochemical Water Oxidation on W-Doped BiVO4 Photocatalysts by Scanning Electrochemical Microscopy. *J. Phys. Chem. C* **2011**, *115*, 12464−12470.
(26) Jia, Q.; Iwashina, K.; Kudo, A. Facile fabrication of an efficient BiVO4 thin film electrode for water splitting under visible light irradiation. *Proc. Natl. Acad. Sci. U. S. A.* **2012**, *109*, 11564−11569.
(27) Chen, L.; Toma, F. M.; Cooper, J. K.; Lyon, A.; Lin, Y.; Sharp, I. D.; Ager, J. W. Mo-Doped BiVO4 Photoanodes Synthesized by Reactive Sputtering. *ChemSusChem* **2015**, *8*, 1066−1071.
(28) Seabold, J. A.; Zhu, K.; Neale, N. R. Efficient solar photoelectrolysis by nanoporous Mo:BiVO4 through controlled electron transport. *Phys. Chem. Chem. Phys.* **2014**, *16*, 1121−1131.
(29) Seabold, J. A.; Choi, K.-S. Efficient and Stable Photo-Oxidation of Water by a Bismuth Vanadate Photoanode Coupled with an Iron Oxyhydroxide Oxygen Evolution Catalyst. *J. Am. Chem. Soc.* **2012**, *134*, 2186−2192.
(30) Kim, T. W.; Choi, K.-S. Nanoporous BiVO4 Photoanodes with Dual-Layer Oxygen Evolution Catalysts for Solar Water Splitting. *Science* **2014**, *343*, 990−994.
(31) Gan, J.; Lu, X.; Rajeeva, B. B.; Menz, R.; Tong, Y.; Zheng, Y. Efficient Photoelectrochemical Water Oxidation over Hydrogen-Reduced Nanoporous BiVO4 with Ni−Bi Electrocatalyst. *ChemElectroChem* **2015**, *2*, 1385−1395.
(32) Choi, S. K.; Choi, W.; Park, H. Solar water oxidation using nickel-borate coupled BiVO4 photoelectrodes. *Phys. Chem. Chem. Phys.* **2013**, *15*, 6499−6507.
(33) Walczak, K.; Chen, Y.; Karp, C.; Beeman, J. W.; Shaner, M.; Spurgeon, J.; Sharp, I. D.; Amashukeli, X.; West, W.; Jin, J.; Lewis, N. S.; Xiang, C. Modeling, Simulation, and Fabrication of a Fully Integrated, Acid-stable, Scalable Solar-Driven Water-Splitting System. *ChemSusChem* **2015**, *8*, 544−551.
(34) Singh, M. R.; Papadantonakis, K.; Xiang, C.; Lewis, N. S. An electrochemical engineering assessment of the operational conditions and constraints for solar-driven water-splitting systems at near-neutral pH. *Energy Environ. Sci.* **2015**, *8*, 2760−2767.
(35) Toma, F. M.; Cooper, J. K.; Kunzelmann, V.; McDowell, M. T.; Yu, J.; Larson, D. M.; Borys, N. J.; Abelyan, C.; Beeman, J. W.; Yu, K. M.; Yang, J.; Chen, L.; Shaner, M. R.; Spurgeon, J.; Houle, F. A.; Persson, K. A.; Sharp, I. D. Mechanistic insights into chemical and photochemical transformations of bismuth vanadate photoanodes. *Nat. Commun.* **2016**, *7*, 12012.
(36) Lichterman, M. F.; Shaner, M. R.; Handler, S. G.; Brunschwig, B. S.; Gray, H. B.; Lewis, N. S.; Spurgeon, J. M. Enhanced Stability and Activity for Water Oxidation in Alkaline Media with Bismuth Vanadate Photoelectrodes Modified with a Cobalt Oxide Catalytic Layer Produced by Atomic Layer Deposition. *J. Phys. Chem. Lett.* **2013**, *4*, 4188−4191.
(37) Kim, T. W.; Choi, K.-S. Improving Stability and Photoelectrochemical Performance of BiVO4 Photoanodes in Basic Media by Adding a ZnFe2O4 Layer. *J. Phys. Chem. Lett.* **2016**, *7*, 447−451.
(38) Green, M. L.; Takeuchi, I.; Hattrick-Simpers, J. R. Applications of high throughput (combinatorial) methodologies to electronic, magnetic, optical, and energy-related materials. *J. Appl. Phys.* **2013**, *113*, 231101.
(39) Muster, T. H.; Trinchi, A.; Markley, T. A.; Lau, D.; Martin, P.; Bradbury, A.; Bendavid, A.; Dligatch, S. A review of high throughput and combinatorial electrochemistry. *Electrochim. Acta* **2011**, *56*, 9679−9699.
(40) Potyrailo, R. A., Maier, W. F., Eds. *Combinatorial and High-Throughput Discovery and Optimization of Catalysts and Materials*; Taylor & Francis: Boca Raton, FL, 2006.
(41) Saito, R.; Miseki, Y.; Nini, W.; Sayama, K. Discovery of Overcoating Metal Oxides on Photoelectrode for Water Splitting by Automated Screening. *ACS Comb. Sci.* **2015**, *17*, 592−599.
(42) Haber, J. A.; Cai, Y.; Jung, S.; Xiang, C.; Mitrovic, S.; Jin, J.; Bell, A. T.; Gregoire, J. M. Discovering Ce-rich oxygen evolution catalysts, from high throughput screening to water electrolysis. *Energy Environ. Sci.* **2014**, *7*, 682−688.
(43) Haber, J. A.; Xiang, C.; Guevarra, D.; Jung, S.; Jin, J.; Gregoire, J. M. High-Throughput Mapping of the Electrochemical Properties of (Ni-Fe-Co-Ce)Ox Oxygen-Evolution Catalysts. *ChemElectroChem* **2014**, *1*, 524−528.
(44) Haber, J. A.; Guevarra, D.; Jung, S.; Jin, J.; Gregoire, J. M. Discovery of New Oxygen Evolution Reaction Electrocatalysts by Combinatorial Investigation of the Ni−La−Co−Ce Oxide Composition Space. *ChemElectroChem* **2014**, *1*, 1613−1617.
(45) Gregoire, J. M.; Xiang, C.; Mitrovic, S.; Liu, X.; Marcin, M.; Cornell, E. W.; Fan, J.; Jin, J. Combined Catalysis and Optical Screening for High Throughput Discovery of Solar Fuels Catalysts. *J. Electrochem. Soc.* **2013**, *160*, F337−F342.
(46) Chemseddine, A.; Ullrich, K.; Mete, T.; Abdi, F. F.; van de Krol, R. Solution-processed multilayered BiVO4 photoanodes: influence of intermediate heat treatments on the photoactivity. *J. Mater. Chem. A* **2016**, *4*, 1723−1728.
(47) Haber, J. A.; Anzenburg, E.; Yano, J.; Kisielowski, C.; Gregoire, J. M. Multiphase Nanostructure of a Quinary Metal Oxide Electrocatalyst Reveals a New Direction for OER Electrocatalyst Design. *Adv. Energy Mater.* **2015**, *5*, 1402307.
(48) Shinde, A.; Guevarra, D.; Haber, J. A.; Jin, J.; Gregoire, J. M. Identification of optimal solar fuel electrocatalysts via high throughput in situ optical measurements. *J. Mater. Res.* **2015**, *30*, 442−450.
(49) Coridan, R. H.; Nielander, A. C.; Francis, S. A.; McDowell, M. T.; Dix, V.; Chatman, S. M.; Lewis, N. S. Methods for comparing the performance of energy-conversion systems for use in solar fuels and solar electricity generation. *Energy Environ. Sci.* **2015**, *8*, 2886−2901.
(50) Trotochaud, L.; Mills, T. J.; Boettcher, S. W. An Optocatalytic Model for Semiconductor−Catalyst Water-Splitting Photoelectrodes Based on In Situ Optical Measurements on Operational Catalysts. *J. Phys. Chem. Lett.* **2013**, *4*, 931−935.
(51) González-Flores, D.; Sánchez, I.; Zaharieva, I.; Klingan, K.; Heidkamp, J.; Chernev, P.; Menezes, P. W.; Driess, M.; Dau, H.; Montero, M. L. Heterogeneous Water Oxidation: Surface Activity versus Amorphization Activation in Cobalt Phosphate Catalysts. *Angew. Chem., Int. Ed.* **2015**, *54*, 2472−2476.
(52) Choi, K.-S.; Jang, H. S.; McShane, C. M.; Read, C. G.; Seabold, J. A. Electrochemical synthesis of inorganic polycrystalline electrodes with controlled architectures. *MRS Bull.* **2010**, *35*, 753−760.
(53) Kang, D.; Kim, T. W.; Kubota, S. R.; Cardiel, A. C.; Cha, H. G.; Choi, K.-S. Electrochemical Synthesis of Photoelectrodes and Catalysts for Use in Solar Water Splitting. *Chem. Rev.* **2015**, *115*, 12839−12887.
(54) Steinmiller, E. M. P.; Choi, K.-S. Photochemical deposition of cobalt-based oxygen evolving catalyst on a semiconductor photoanode for solar oxygen production. *Proc. Natl. Acad. Sci. U. S. A.* **2009**, *106*, 20633−20636.
(55) Zhong, D. K.; Cornuz, M.; Sivula, K.; Gratzel, M.; Gamelin, D. R. Photo-assisted electrodeposition of cobalt-phosphate (Co-Pi) catalyst on hematite photoanodes for solar water oxidation. *Energy Environ. Sci.* **2011**, *4*, 1759−1764.

DOI: 10.1021/acsami.6b06714
ACS Appl. Mater. Interfaces 2016, 8, 23696−23705